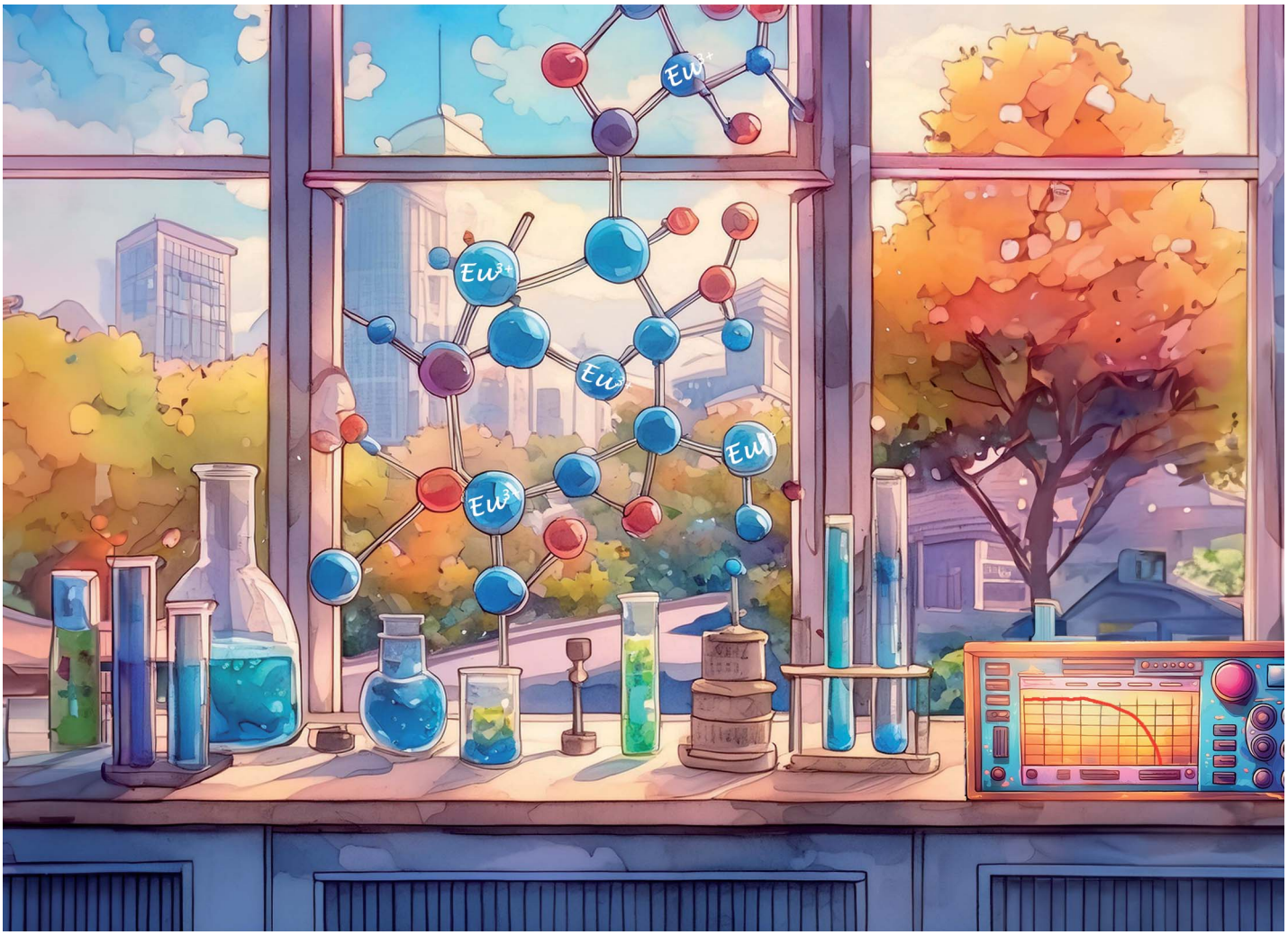

Highlighting research on Europium-based Luminescent Solar Concentrators (LSCs) by Professor Lidia Armelao's group. The group comprises researchers from both the Department of Chemical Sciences at the University of Padova, Italy, and the Institute for Condensed Matter Chemistry and Energy Technologies (ICMATE) of the National Research Council of Italy.

Transparent and colour-neutral luminescent solar concentrators using bright Eu^{3+} supramolecular cages towards photovoltaic windows

Super-bright $[Eu_2L_4]^{2-}$ cages bearing bis-β-diketonate ligands are employed to develop transparent and colourless Luminescent Solar Concentrators. Their aesthetic characteristics make them promising for a seamless integration into buildings as photovoltaic windows able to block UV light and exploit it to produce energy.

As featured in:

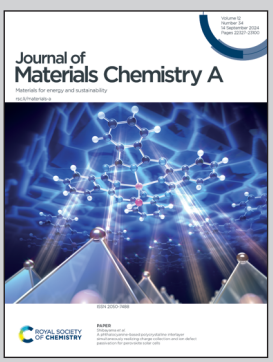

See Bottaro *et al.*,
J. Mater. Chem. A, 2024, **12**, 22516.

ROYAL SOCIETY OF CHEMISTRY

rsc.li/materials-a

Registered charity number: 207890

Journal of Materials Chemistry A

ROYAL SOCIETY OF CHEMISTRY

PAPER

View Article Online
View Journal | View Issue

Cite this: J. Mater. Chem. A, 2024, 12, 22516

Transparent and colour-neutral luminescent solar concentrators using bright Eu^{3+} supramolecular cages towards photovoltaic windows†

Irene Motta, [a] Gregorio Bottaro, *[bc] Maria Rando, [a] Marzio Rancan, *[bc] Roberta Seraglia[d] and Lidia Armelao [ace]

The integration of photovoltaic (PV) devices into the built environment has become a key factor for the development of energy efficient buildings. Luminescent solar concentrators (LSCs) are well suited for this application, as they could be installed over architectural elements inaccessible to conventional PVs. In the present work, we report the synthesis of super-bright $[Eu_2L_4]^{2-}$ cages bearing bis-β-diketonate ligands and their subsequent embedding in polymethylmethacrylate (PMMA) by casting of 5 × 5 × 0.27 cm^3 planar LSCs. With a measured average visible transmittance (AVT) of 92%, the proposed LSCs possess excellent transparency and aesthetic quality fit for glass destined for neutral colour applications. Moreover, the obtained materials absorb from 60% to 90% of solar UV radiation, exposure to which is harmful for human health and responsible for fading of building interiors. The performance of devices attained by edge-coupling LSC slabs with monocrystalline silicon solar cells matches that of classic Eu^{3+}-based concentrators. Nonetheless, the employment of super-bright $[Eu_2L_4]^{2-}$ luminophores allows the reduction of the Eu^{3+} ion content of our devices down to 0.01% wt. This denotes a most efficient use of a valuable material like europium in the developed LSC-PVs, as Eu^{3+} weight contents reported in relevant literature were one to two orders of magnitude higher.

Received 9th May 2024
Accepted 30th May 2024

DOI: 10.1039/d4ta03244f

rsc.li/materials-a

Introduction

Developing energy-efficient infrastructures towards decarbonisation of buildings[1,2] requires innovative renewable energy technologies. Among these, building-integrated photovoltaics aim to directly integrate PV systems into constructions as a replacement for conventional building components.[3] Luminescent solar concentrators (LSCs) are light-management devices that have largely been proposed for the realization of transparent or semi-transparent BIPVs.[4–8] They consist of slabs of glassy or polymeric material doped or coated with luminescent species (luminophores), whose emission can be stimulated by sunlight incident on the slate's surface. The emitted radiation is then waveguided towards the edges of the device, where thin strips of conventional PV material collect it and convert it into electrical power (Fig. 1a). The versatility in materials, shapes and coloration makes LSCs suitable for installation over a wide range of architectures, where constrains in terms of functionality and appearance limit or prevent the introduction of classic PV modules. This becomes especially true in the case of windows, for which tunability in colour and transparency is highly requested. The latest efforts in designing LSCs suitable for photovoltaic windows have been directed towards highly transparent and colourless materials, to ensure seamless integration in most buildings destined for housing and working.[3,9–12] Provided the use of highly transparent matrices, among which PMMA is the most popular option in LSC studies, the choice of luminophore plays a determinant role in the appearance and optical quality of the LSC. While a broad absorption spectrum is generally a desirable feature in LSC emitters, absorption of visible light reaches a trade-off with the coloration of the device. Therefore, UV or NIR selective absorbers are necessary to produce low- or non-tinted materials. Lanthanide antenna complexes (Fig. 1b) are suitable candidates to obtain transparent and colourless LSCs, as the ligand absorption range covers, in most cases, the UV spectral region.[13] This class of luminophores presents other advantages, such as intense sensitized emission and very large pseudo-Stokes shifts

[a]Department of Chemical Sciences (DiSC), University of Padova, via F. Marzolo 1, 35131, Padova, Italy
[b]Institute of Condensed Matter Chemistry and Technologies for Energy (ICMATE), National Research Council (CNR), c/o Department of Chemical Sciences (DiSC), University of Padova, via F. Marzolo 1, 35131, Padova, Italy
[c]National Interuniversity Consortium of Materials Science and Technology (INSTM), Florence, Italy
[d]Institute of Condensed Matter Chemistry and Technologies for Energy (ICMATE), National Research Council (CNR), Corso Stati Uniti, 4, 35127, Padova PD, Italy
[e]Department of Chemical Sciences and Materials Technologies (DSCTM), National Research Council (CNR), Piazzale A. Moro 7, 00185, Roma, Italy

† Electronic supplementary information (ESI) available. CCDC 2349361 and 2349362. For ESI and crystallographic data in CIF or other electronic format see DOI: https://doi.org/10.1039/d4ta03244f

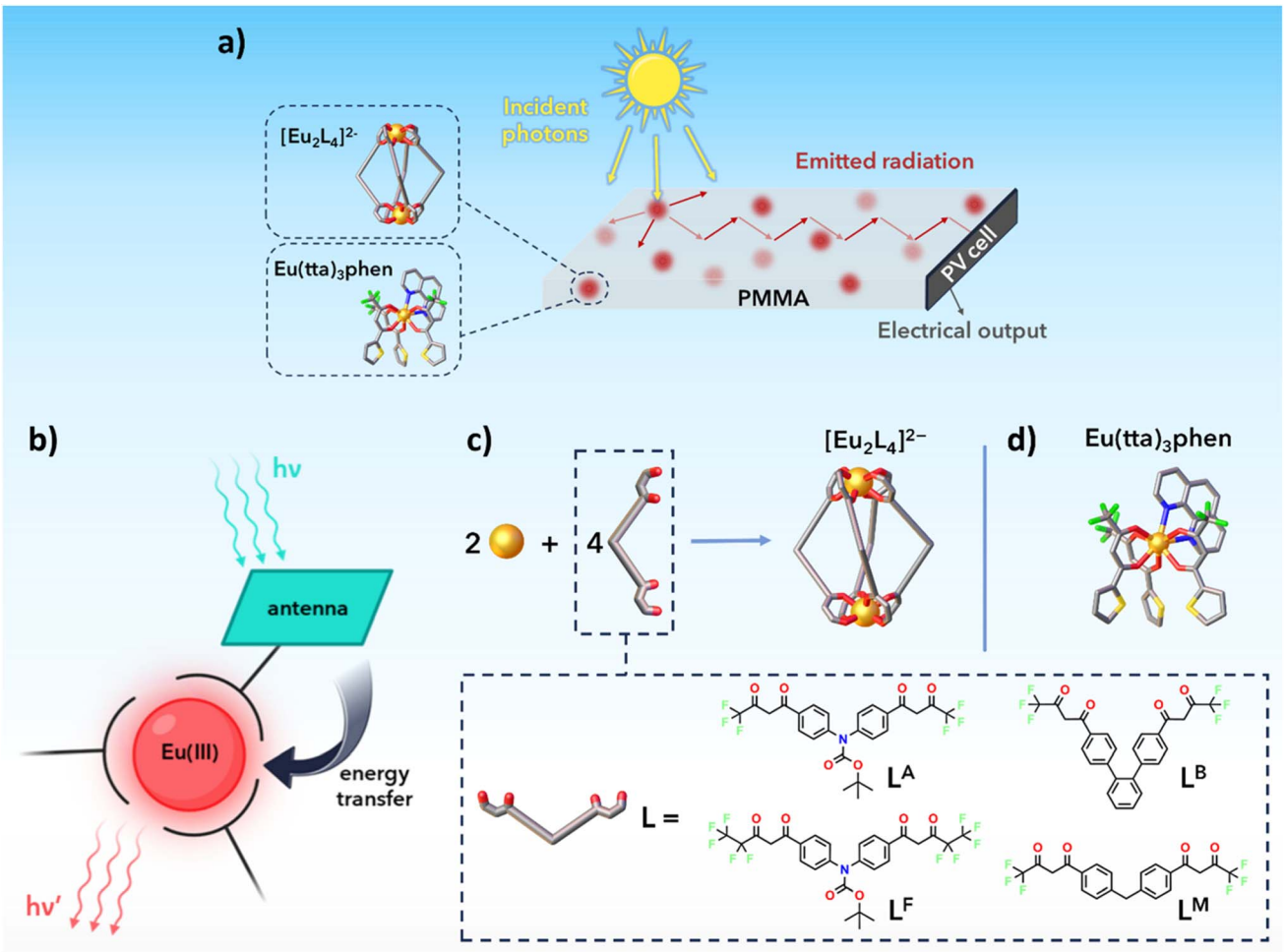

Fig. 1 (a) Working mechanism of the proposed Eu^{3+}-based transparent luminescent solar concentrators. (b) Schematization of the antenna effect in a generic Eu^{3+} complex. The main steps involved in the Ln^{3+} sensitized emission are absorption of UV light by the organic ligands (the antenna), Inter-System Crossing (ISC) from the antenna's singlet excited state to its triplet excited state, intramolecular energy transfer (ET) towards the ion's emissive excited state and finally metal-centred emission. (c) Self-assembly of the $[Eu_2L_4]^{2-}$ cages and molecular structures of the employed ligands. (d) Structure of the $Eu(tta)_3phen$ complex.

(>200 nm). Zero overlap between the luminophore absorption and emission is highly desirable for LSC scale-up, since re-absorption losses are one of the main drawbacks encountered with larger modules, thus hindering their development beyond the lab-scale.[6,14]

Complexes of rare earth ions with β-diketonates have become a widespread choice due to the versatility in molecular design conferred by this class of ligands, and the relative ease in their synthesis and functionalization.[15,16] The literature on lanthanide-based LSCs is mainly centred on β-diketonates,[17–19] and more specifically Eu^{3+} and Tb^{3+} since they display the highest photoluminescence quantum yields (PLQY) among the rare earth series.[20]

Herein, we report the synthesis and characterization of highly transparent LSCs based on a series of supramolecular, binuclear lanthanide bis-β-diketonates with the general formula $[Ln_2L_4]^{2-}$ ($L = L^A$, L^B, L^M, L^F) and structure depicted in Fig. 1c. $Eu(tta)_3phen$ (tta = thenoyltrifluoroacetone and phen = 1,10-phenanthroline, Fig. 1d) is also included in the study, due to its documented use in the literature regarding lanthanide-based LSCs.[17,18] PMMA has been adopted as the host medium, due to its high transmittance in the UV and in the visible region. Emitters have been dissolved in a methyl methacrylate (MMA)/PMMA syrup that has been then poured into a casting mould and successively polymerized to prepare the LSCs. Spectroscopic characterisation of the luminophores has been conducted before and after embedment in the polymeric matrix. Average visible transmission (AVT), colour rendering index (CRI) and CIELAB coordinates have been derived from the transmittance spectra of the fabricated LSCs. The prepared LSCs were used to study the behaviour of the devices obtained by edge-coupling the luminescent planar waveguides with monocrystalline Si solar cells. Device performances have been evaluated according to the latest published protocols[21,22] and terminology[23] used in LSC research. A perspective on the literature regarding Eu^{3+}-based concentrators is also offered, with the aim to assess the stand of the present study over the past-decade results.

Experimental

Experimental details for luminophore synthetic procedures, single crystal X-ray diffraction and mass spectrometry are given in the ESI.†

LSC fabrication

The LSCs have been prepared through bulk radical polymerization of methyl methacrylate (MMA) solutions containing the desired amount of luminophore, 20 wt% of commercial polymethylmethacrylate powder (PMMA, AMW = 350 000 g mol^{-1}) and 0.1 wt% of azobisisobutyronitrile (AIBN). The polymerization has been conducted in a water bath set at 60 °C for 18 hours, where the casting solution had previously been transferred into a casting mold composed of two glass plates clamped together, separated by a PVC plastic gasket. After extraction of the polymerised tile from the mold, the gasket has been cut off and the edges have been polished to yield the finished LSC.

Photophysical characterization

UV/vis absorption spectra were recorded on a CARY5000 double-beam spectrophotometer in the 300–800 nm range, with a spectral bandwidth of 2 nm. Transmittance ($T(\lambda)$) and reflectance ($R(\lambda)$) spectra were recorded on the same instrument, equipped with a poly(tetrafluoroethylene)-coated integration sphere, and with the same parameters. Absorptance ($A(\lambda)$) spectra have been calculated as $A(\lambda) = 1 - T(\lambda) - R(\lambda)$.

Photoluminescence spectra were collected on a Horiba JobinYvon Fluorolog-3 spectrofluorimeter equipped with double-grating monochromators on the excitation side and iHR320 spectrograph on the emission side. A R928P Hamamatsu photomultiplier or Horiba Sincerity CCD detectors were employed. A 450 W Xe arc lamp was used as the excitation source. PLQY measurements were performed on the same instrument equipped with a poly(tetrafluoroethylene)-coated integration sphere, using a 90° excitation-collection geometry.

Electrical characterization

Current–voltage (I–V) curves of the LSC-PVs were collected under simulated solar irradiation (100 mW cm^{-2}, AM1.5G) with a Keithley 2450 Graphical Source Measure Unit (SMU). Monocrystalline Si cells coupled to the LSCs were purchased from IXYS Corporation (series IXOLAR™ SolarBIT, model KXOB22-12X1F). External quantum efficiency (EQE) measurements were performed on a custom-assembled setup, composed of a UV/vis transmitting optical fibre (Ocean Insight QP1000-2-UV/Vis, 300–1100 nm) coupled to the Horiba JobinYvon Fluorolog-3 spectrofluorimeter, and an appropriate sample and PV cell holder. Incident light was focused on the LSC surface (spot diameter 1 mm) through a lens doublet. The focusing optics have been mounted on a XYZ linear stage allowing alignment of the light spot and scanning over the whole sample surface (25 mm^2). Incident power readings were acquired through a Gentec-EO Pronto Si power meter, while current readings were collected with a Keithley 2450 Graphical SourceMeter SMU. In both J–V and EQE measurements, LSCs and Si cells were optically coupled with optical grade silicone grease.

Results and discussion

Luminophore synthesis

Ligands L^B, L^M and L^A (Fig. 1c) were prepared as previously reported.[24,25] The ligand L^F (Fig. 1c) is a modified version of L^A bearing an additional $-CF_2-$ unit in the fluorinated terminal chains, to increase the cage solubility. This new ligand was prepared by a two step procedure (Cu(I) catalysed N–C coupling reaction followed by Claisen condensation) and fully characterized by NMR (Fig. 2a), single crystal XRD (Fig. S1 and Table S1†) and electrospray mass spectrometry (ESI-MS, Fig. S3†). Deprotonation of the ligand with tetraethylammonium hydroxide (TEAOH) and subsequent addition of a Eu^{3+} inorganic salt leads to the self-assembly of quadruple-stranded cages. We already reported elsewhere[24,25] the detailed synthesis and characterization (NMR, ESI-MS and single crystal XRD) for the cages based on L^B, L^M and L^A. The synthesis and characterization of the new $\{[Eu_2L^F{}_4](NEt_4)_2\}$ cage is here discussed. The formation of the cage has been followed and assessed through ^{1}H-NMR spectroscopy. The spectra of the ligand (H_2L^F, $L^{F\,2-}$) and $[La_2L^F{}_4]^{2-}$ analogue are displayed in Fig. 2a. Upon deprotonation, all ligand signals experience an upfield shift. The most pronounced effect is seen in proton H1, located at the α position of the β-diketonate moiety. Following La^{3+} ion coordination, the cage exhibits a single set of signals, consistent with the ligand's C_2 symmetry and the mean C_4 symmetry of the quadruple-stranded $[La_2L^F{}_4]^{2-}$ architecture. To provide dimensional information, diffusion-ordered NMR spectroscopy (DOSY) was conducted, as shown in Fig. 2b. The calculated hydrodynamic diameter for $[La_2L^F{}_4]^{2-}$ is 22.2 Å. The Eu^{3+} cage gives a very clean ESI-MS spectrum with only one signal due to the $[Eu_2L^F{}_4]^{2-}$ double-negative charged species (Fig. 2c). The crystal structure of the newly synthetized $\{[Eu_2L^F{}_4](NEt_4)_2\}$ has been determined by single-crystal X-ray diffraction (Fig. 2d and S2†). The H···H distances of the *tert*-butyl groups of opposite ligands are in the range 21.3–22.8 Å. This value agrees with the hydrodynamic diameter calculated from the DOSY experiment (22.2 Å) for the La^{3+} cage. As previously observed for the $[Eu_2L^M{}_4]^{2-}$, $[Eu_2L^B{}_4]^{2-}$ (ref. 24) and $[Eu_2L^A{}_4]^{2-}$ cages,[25] one of the two tetraethylammonium cations is hosted by the quadruple stranded cage. In such quadruple-stranded Ln^{3+} cages, the ligand scaffold and guest molecule can influence the formation of helicates or mesocates.[26] The cage $[Eu_2L^F{}_4]^{2-}$ is a helicate with both the right-handed (P, ΔΔ) and left-handed (M, ΛΛ) isomers in a 1 : 1 ratio in the unit cell. Finally, the crystal structure evidences that the two Eu centres have different coordination numbers (Fig. 2d). Both the ions are tetrakis-chelated by four β-diketonate groups, but Eu_2 also has the ninth site occupied by an ethanol molecule. We previously[25] calculated that solvent molecules such as water and ethanol are loosely bonded to the Ln^{3+} ion and hence can be present or absent according to the experimental conditions. Tables S2 and S3† report the result of the stereochemical analysis by means of continuous shape measures[27] showing that the eight-

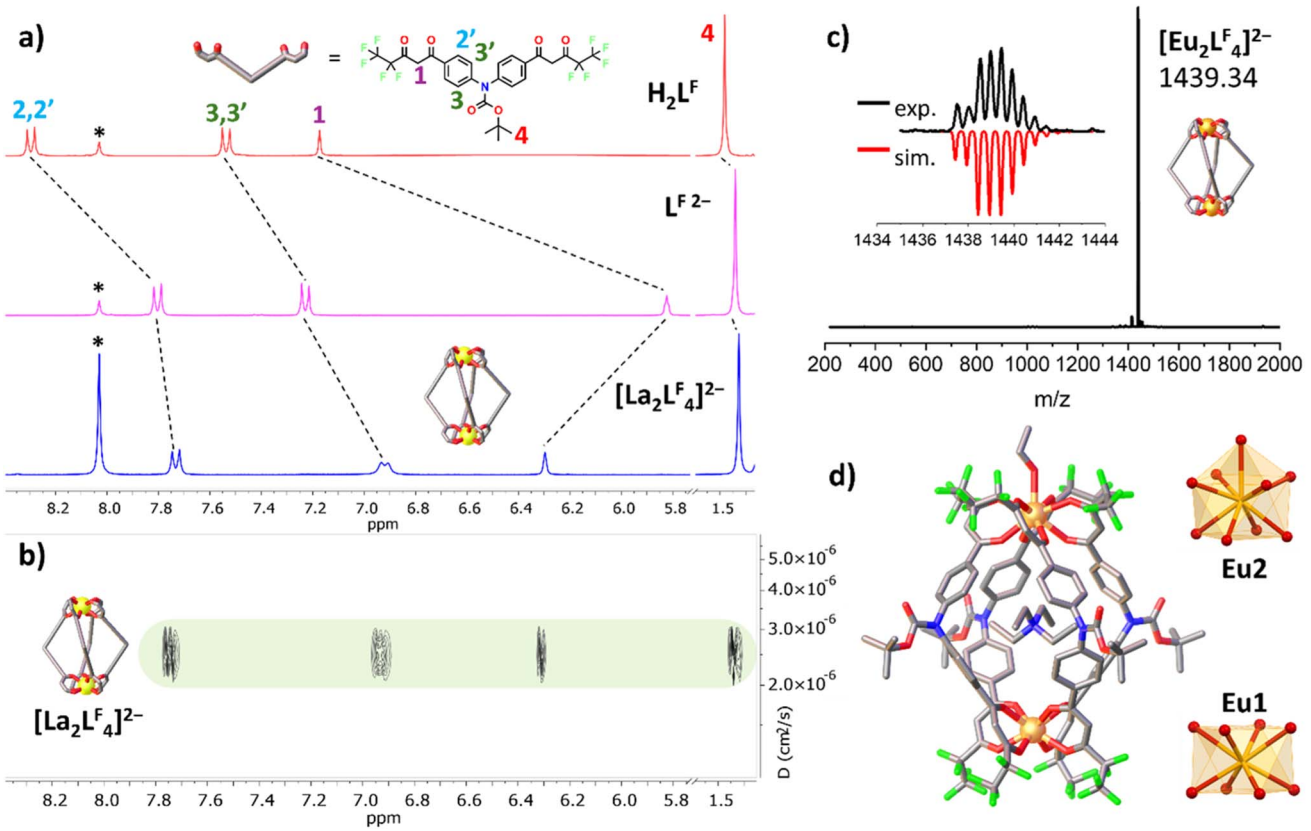

Fig. 2 (a) ^{1}H-NMR spectra (25 °C, 300 MHz, DMF-d_7) of ligand H_2L^F, deprotonated ligand $L^{F\,2-}$ and the cage $[La_2L^F_4]^{2-}$ (* = DMF). (b) DOSY of $[La_2L^F_4]^{2-}$. (c) ESI-MS spectrum of the $\{[Eu_2L^F_4](NEt_4)_2\}$ cage. Inset: experimental (black) and simulated (red) isotopic patterns. (d) Crystal structure of the $\{[Eu_2L^F_4](NEt_4)_2\}$ cage (helicate *M*, ΛΛ form) and coordination polyhedra for Eu1 and Eu2. H atoms and the external NEt_4^+ ion were omitted for clarity. Color code: C, grey; O, red; N, blue; F, green; Eu, orange; La, yellow.

coordinated centre has a square antiprismatic coordination geometry while the nine-coordinated ion has a capped square antiprismatic coordination geometry (Fig. 2d).

The synthesis of Eu(tta)$_3$phen comprised a first deprotonation of tta using NaOH and consequent addition of the Eu^{3+} salt to the mixture of phen and deprotonated tta. The desired product was obtained by employing a metal : tta : NaOH : phen molar ratio of 1 : 3 : 3 : 1. ESI-MS (Fig. S4†) confirmed the nature of the synthesised product.

Absorption and emission in MMA solutions

The photophysics of the luminophores has been first investigated in MMA, since it is the reaction solvent used in the preparation of the LSCs.

UV/vis absorption and photoluminescence (PL) spectra (Fig. 3a) have confirmed effective sensitization through the antenna effect: absorption of light is carried out entirely by the β-diketonate ligands in the 300–380 nm region, resulting in a ligand-centred excitation, while the sole PL profile observed is that of the Eu^{3+} ion. The Eu^{3+} PL spectrum is composed of five sharp peaks, corresponding to the transitions originating from the $^5D_0$ excited state towards the ^7F_J ($J = 0$, 1, 2, 3, and 4) ground state. The $^5D_0 \rightarrow {}^7F_2$ hypersensitive transition at 612 nm dominates the emission spectrum of Eu^{3+} β-diketone complexes and is responsible for the red luminescence.[15,28] Overlap between absorption and emission is null, with a pseudo-Stokes shift of ≈200 nm.

When selecting the most promising luminescent complexes/molecules for the development of LSCs, we must consider both the values of the photoluminescence quantum yield (PLQY) and the absorption coefficient (ε). Often, seeking the best emitters, there is a tendency to consider only the PLQY. However, this is a partial evaluation since it only takes into account the fraction of emitted photons but does not provide information on the number of absorbed photons (indicated by ε). The parameter that should be maximized is the number of photons emitted per unit area and per unit time. For molecules and complexes in solution, this parameter is well represented by the brightness ($B = \varepsilon \times$ PLQY),[29,30] *i.e.*, the product of the absorption coefficient and the emission quantum yield. The luminophores here discussed have similar absorption and emission spectra and hence it is sufficient to compare the brightness values relative to the maximum absorption (Fig. 3b and Table 1). In MMA solutions, $[Eu_2L^B_4]^{2-}$ is the brightest complex of the family with B = 96 880 M^{-1} cm^{-1}, followed by $[Eu_2L^A_4]^{2-}$ and $[Eu_2L^F_4]^{2-}$, having a B of around 70 000 M^{-1} cm^{-1}, and then $[Eu_2L^M_4]^{2-}$ with B close to 45 000 M^{-1} cm^{-1}. The difference in brightness between Eu(tta)$_3$phen (13 500 M^{-1} cm^{-1}) and the binuclear lanthanide

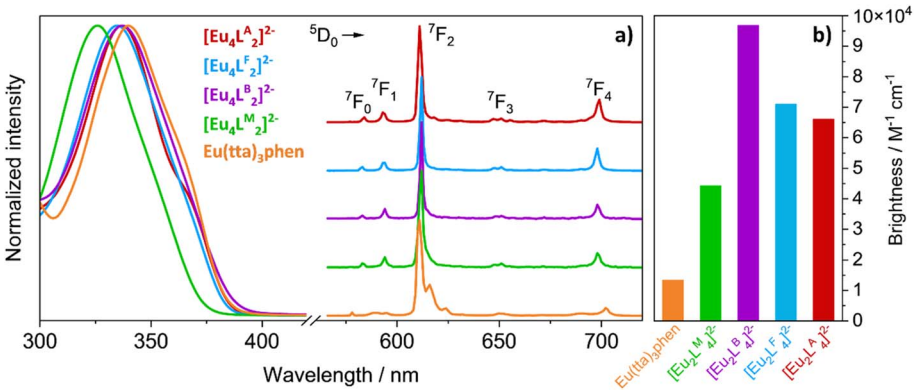

Fig. 3 (a) Normalized absorption and emission spectra of 1×10^{-5} M solutions of the luminophores in MMA. (b) Histogram displaying the brightness at λ_{max} of the investigated luminophores in MMA solutions. Color code: orange = $Eu(tta)_3phen$, green = $[Eu_2L^M_4]^{2-}$, purple = $[Eu_2L^B_4]^{2-}$, light blue = $[Eu_2L^F_4]^{2-}$, and red = $[Eu_2L^A_4]^{2-}$.

Table 1 Molar extinction coefficient (ε_{max}), photoluminescence quantum yield (PLQY) and molar brightness (B) values collected for 1×10^{-5} M solutions of the luminophores in MMA. Maximum solubility achieved for the luminophores in MMA. The values of PLQY and absorption coefficients relative to the luminophores embedded in PMMA are reported in parentheses

	$\varepsilon_{max} \times 10^5/M^{-1}$ cm^{-1}	PLQY	B/M^{-1} cm^{-1}	Solubility/mM
$[Eu_2L^A_4]^{2-}$	1.61 (1.65)	0.41 (0.39)	66 010	0.0184
$[Eu_2L^F_4]^{2-}$	1.42 (1.43)	0.50 (0.53)	71 000	0.321
$[Eu_2L^B_4]^{2-}$	1.73 (—[a])	0.56 (—[a])	96 880	0.0195
$[Eu_2L^M_4]^{2-}$	1.01 (—[a])	0.48 (—[a])	48 480	0.0216
$Eu(tta)_3phen$	0.50 (0.53)	0.27 (0.25)	13 500	5.02

[a] PLQY and ε_{max} were not measured for these samples in the polymeric matrices because $[Eu_2L^B_4]^{2-}$ and $[Eu_2L^M_4]^{2-}$ give rise to issues during material synthesis and were not employed to develop LSC devices (for details see LSC preparation and characterization section).

bis-β-diketonates $[Eu_2L_4]^{2-}$ (L = L^A, L^B, L^M) is noteworthy, reaching about one order of magnitude. Considering the brightness values in MMA solutions, the most promising candidate for the development of LSCs seems to be $[Eu_2L^B_4]^{2-}$. Prior to material synthesis and characterization, we investigated the compatibility of the complexes with the PVC gasket used as lateral walls of the LSC casting mould employed for MMA polymerization. Gasket strips (approximately $1 \times 3 \times 0.3$ cm^3) were immersed in MMA solutions of the investigated luminophores, at the same concentrations used for LSC castings. After 20 h (approximately the polymerization time) the PVC pieces were removed from the solutions, dried at room temperature and observed under a UV lamp at 365 nm to detect eventual traces of the cages. The PVC strip immersed in the $[Eu_2L^B_4]^{2-}$ solution displayed a markedly brighter luminescence with respect to the others, suggesting a strong affinity between $[Eu_2L^B_4]^{2-}$ and PVC and eventually possible issues during material synthesis. Moreover, we observed that solubility of $Eu(tta)_3phen$ in MMA is about two orders of magnitude larger than those of $[Eu_2L^A_4]^{2-}$, $[Eu_2L^B_4]^{2-}$ and $[Eu_2L^M_4]^{2-}$ (Table 1). To address this aspect, we synthesized ligand L^F by slightly modifying L^A in order to obtain higher cage solubility in MMA, achieving in the end a twenty-fold increase in it. Once again, the compatibility of the corresponding bright europium complex, $[Eu_2L^F_4]^{2-}$, with the PVC gasket was investigated, detecting no type of interaction.

LSC preparation and characterization

All luminophores have been incorporated into PMMA through a water bath casting procedure with the use of an appropriate casting mould (see the Experimental section) to prepare planar square LSCs with an active area of 5×5 cm^2 and thickness of 0.27 cm. A geometric gain (G) of 4.63 has been calculated through eqn (1), where A_{in} is the incident solar irradiance area, also referred to as the LSC active area, and A_{out} is the light collection area, usually the area of the LSC edges.[23]

$$G = \frac{A_{in}}{A_{out}} \quad (1)$$

An active area of 25 cm^2 has been chosen because it has been proposed as a reasonable standard size for easily comparing results between independent LSC studies on a laboratory scale.[22,31] The amount of available luminophores for the castings depended on their solubility in MMA, which was found to be largely different in the investigated luminophores. Maximum solubilities achieved for $Eu(tta)_3phen$ and $[Eu_2L^F_4]^{2-}$ in MMA were 0.5 wt% and 0.1 wt%, respectively, while those of the other cages $[Eu_2L^A_4]^{2-}$, $[Eu_2L^B_4]^{2-}$ and $[Eu_2L^M_4]^{2-}$ were two orders of magnitude lower. Five samples have hence been prepared using each system at 0.005 wt%, and an additional LSC has been prepared for both $Eu(tta)_3phen$ and $[Eu_2L^F_4]^{2-}$ at their solubility

limit. An undoped PMMA tile has also been fabricated. Labelling of the prepared LSCs is reported in Table S4.†

Absorption spectra of the luminophores in PMMA (Fig. 4a) match the absorbance profiles collected for the MMA solutions. Upon UV excitation at $\lambda = 365$ nm, all LSCs displayed bright red luminescence and concentration of the emitted light on the tiles edges (Fig. 4b–d). The same light guiding properties could already be appreciated by the naked eye for all doped LSCs under daylight (Fig. 4e and f).

Since the Eu^{3+} emission spectrum is sensitive to the ion's coordination site[28] and displays different shapes accordingly, such a feature has been adopted as a qualitative tool to detect possible alterations in the luminophores' structure caused by embedment into the PMMA matrix. The PL profiles recorded for LSCs and solutions well agree with one another for all the investigated Eu^{3+} complexes, meaning that neither the PMMA matrix nor material processing affects the structural integrity of such luminophores. Accordingly, absorption coefficients and PLQY are fully consistent between solutions and PMMA tiles (Table 1). The resultant **LSC-A**, **LSC-F** and **LSC-T** were homogeneous and defect-free. Instead, **LSC-B** showed luminophore segregation towards its edges, as observed under 365 nm excitation (Fig. 4c). Such spatial distribution was ascribed to a preferential absorption of the luminophore into the PVC gasket used to seal the casting mould, thus determining loss of control over the loading of $[Eu_2L^B_4]^{2-}$ into PMMA. This behaviour was already presumed by the reported preliminary PVC swelling tests. When illuminated with UV light, **LSC-M** (Fig. 4d) exhibits several bright spots dispersed randomly throughout the polymeric matrix. These bright spots are due to the precipitation of $[Eu_2L^M_4]^{2-}$, likely occurring during polymerization, within the matrix. Such behaviours make these complexes not suitable for device development. We emphasize that material processing may affect single luminophores differently, despite small differences in the molecular structure of the ligands as in the present case. The solubility increase obtained by introducing a $-CF_2-$ moiety in the terminal chain of the L^A ligand (Fig. 1c) is noteworthy. Hence, the suitability of an emitter for the LSC application should be evaluated based on its characterization after embedment into the matrix of choice.

Considering the application field of the studied materials, their aesthetic appearance is of paramount importance, especially if they are intended as replacements for residential or shop windows. The parameters used to quantitatively assess this aspect are (i) the Average Visible Transmittance (AVT), which measures the amount of visible light transmitted by the LSC, (ii) the Colour Rendering Index (CRI), which quantifies how accurately the colours of objects are reproduced when illuminated with a particular light source, and (iii) (a^*, b^*) CIELAB coordinates, which define the colour of the material in a perceptually uniform space (a^* gives the colour variation along the green-red axis and b^* along the yellow-blue one). For the determination of these parameters, AM1.5G and AM1.5G $\times$ $T(\lambda)$ ($T(\lambda)$ being the transmittance spectrum of the material) are used as source spectra.[32]

Fig. 5a shows the UV/vis transmittance spectra of the $[Eu_2L^A_4]^{2-}$, $[Eu_2L^F_4]^{2-}$ and $Eu(tta)_3phen$ doped LSCs, as well as that of undoped PMMA. The fabricated LSCs show very high transparency, as they transmit all visible light with AVT $\approx$ 92%. They also determine minimal visual impact on the transmitted light, as calculated CRI values are above 98 for all samples (Table S5†).

A recent survey on a wide inventory of commercially available and mass-market glass products has provided reference key

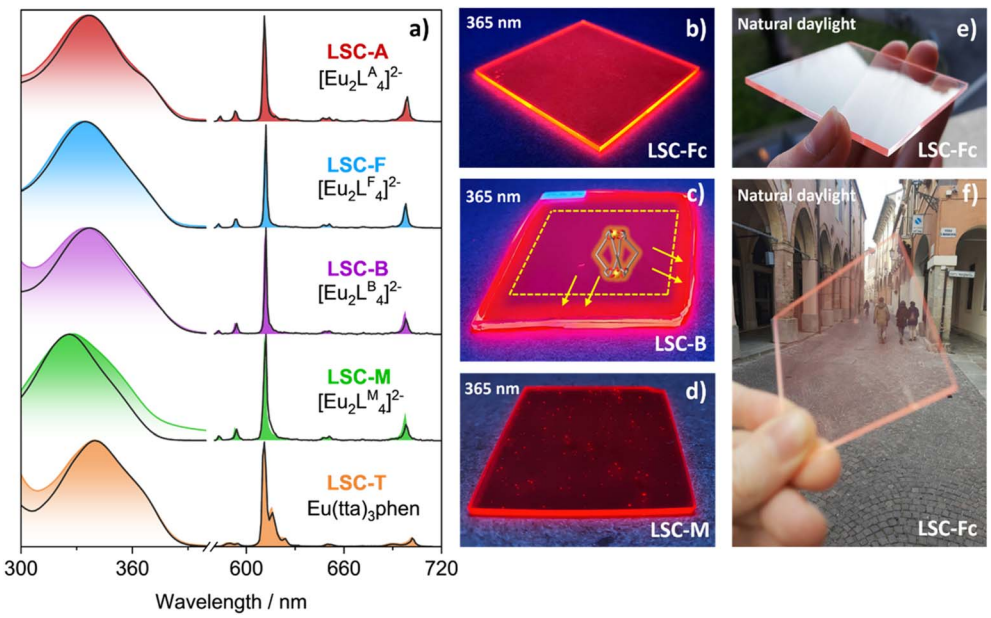

Fig. 4 (a) Normalized absorption and emission spectra of LSCs containing different luminophores at 0.005 wt% (filled colours), superimposed on normalized absorption and emission spectra of the corresponding 1×10^{-5} MMA solutions (black solid line). (b) **LSC-Fc**, (c) **LSC-B** and (d) **LSC-M** under 365 nm UV illumination. (e and f) **LSC-Fc** directly exposed to natural daylight.

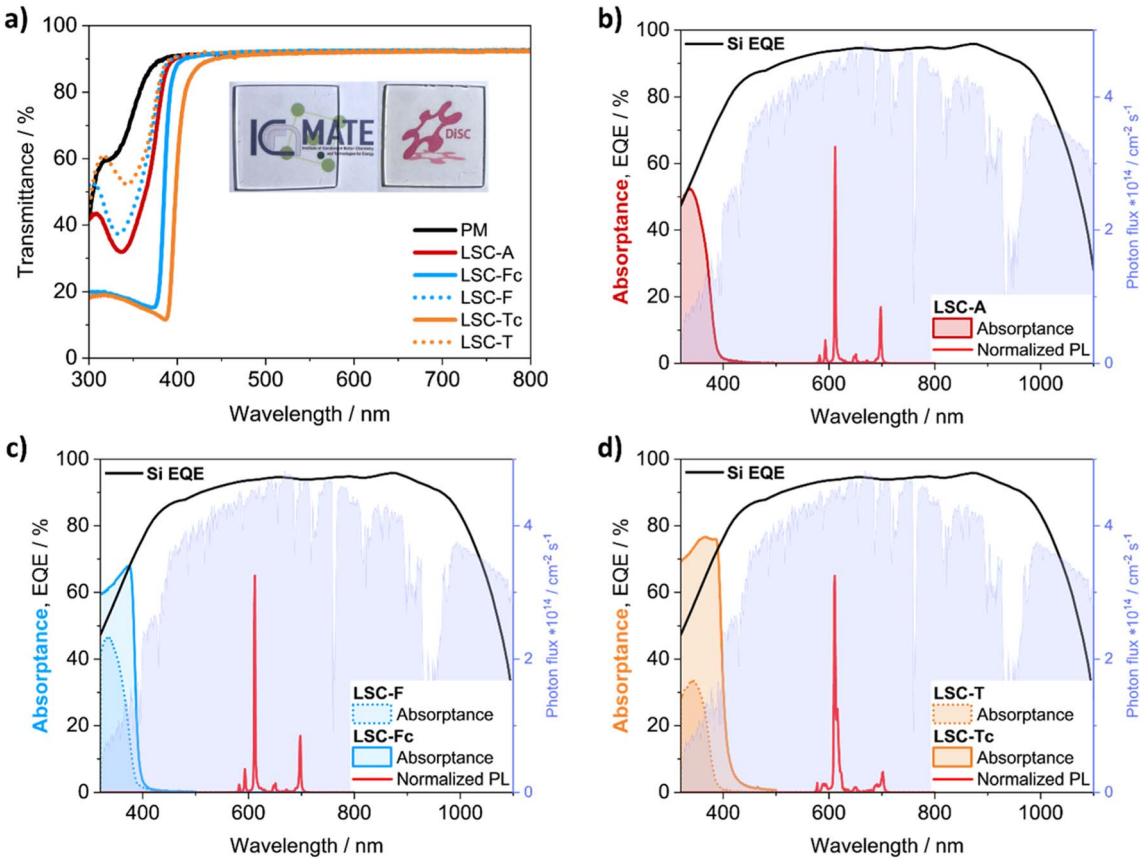

Fig. 5 (a) Transmittance spectra recorded for the selected LSCs (inset: **LSC-Tc** under white LED illumination, over printed ICMATE and DiSC logos). (b–d) Absorptance and normalized PL spectra of the selected LSCs superimposed on the employed Si cell EQE curve and to the AM1.5G solar photon flux.

levels for the aesthetic quality of transparent window products in the glazing industry.[10] A CRI ≥ 85, and CIELAB coordinates of $-7 < a^* < 0$ and $-3 < b^* < 7$ have been found as acceptable standards for products destined for neutral colour applications. Besides presenting (a^*, b^*) coordinates widely within the specified intervals, our samples possess excellent colour and imaging fidelity, where the attribute "excellent" refers to CRI values falling within the 95–100 interval.[10] Furthermore, the whole series of doped LSCs shows a CRI and CIELAB coordinates comparable to those of plain PMMA, indicating that the presence of the luminophores does not modify the visible appearance and the light transmitting properties of the pristine material.

The optimal aesthetic quality of the LSCs containing $[Eu_2L^F_4]^{2-}$ and $Eu(tta)_3phen$ remains unchanged even at higher luminophore loadings. **LSC-Fc** and **LSC-Tc** both retain high transparency and absence of heavy coloration while a higher luminophore content of 0.1 wt% and 0.5 wt%, respectively, allows them to harvest more light on a wider portion of the UV region and is responsible for a larger total absorptance (eqn (2) and (3)) over the less concentrated samples (Table S5†). Absorption onsets, in fact, shift from 380 nm up to 395 nm and 410 nm, respectively. To better evidence the light absorption capability of the materials it is convenient to refer to the total absorptance $\eta_{s,abs}$, defined as follows:[23,33]

$$\eta_{s,abs} = n_s^{-1} \times \int_s A(\lambda) \times \Phi_{ph}^{AM1.5G}(\lambda) d\lambda \quad (2)$$

$$n_s = \int_s \Phi_{ph}^{AM1.5G}(\lambda) d\lambda \quad (3)$$

where $A(\lambda)$ is the absorptance profile of the LSC (Fig. 5b–d), $\Phi_{ph}^{AM1.5G}(\lambda)$ is the AM1.5G photon flux and n_s is its integral. $A(\lambda)$ has been calculated from the transmittance and reflectance spectra, both acquired using an integrating sphere, by applying the photon balance equation $A(\lambda) + T(\lambda) + R(\lambda) = 1$. The integration is performed over the whole AM1.5G spectrum. It becomes evident that achieving a high luminophore concentration is crucial for a more efficient light absorption (Fig. 5b–d).

LSC-Fc and **LSC-Tc** have $\eta_{s,abs}$ values of 1.11% and 1.81% (eqn (2) and (3)), respectively, enabling them to absorb up to 90% of the available UV photons. Notably, UV photons in the 280–400 nm range constitute only about 2% of the AM1.5G spectrum when expressed in terms of photon flux.

Given the large gap between absorbing and emitting regions displayed by the investigated LSCs (Fig. 4 and 5), the possibility of self-absorption losses, arising from the sensible luminophore loading increase in **LSC-Fc** and **LSC-Tc**, can be safely excluded.

Consequently, these two samples are expected to produce significantly higher electrical outputs when coupled to Si cells in the LSC-PV configuration with respect to their less concentrated analogues. Additionally, UV-blocking capabilities are highly desirable for residential and shop windows to prevent fading of furniture, artwork, and flooring. This is typically achieved by applying passive window treatments that function solely by absorbing UV light. Luminescent solar concentrators based on europium antenna complexes offer an innovative approach, transforming passive elements into active ones by converting blocked UV radiation into visible light while also generating electricity.

Device characterization

As previously stated, all functional characterization studies have been conducted in compliance with the guidelines published in recent literature regarding luminescent solar concentrators.[21,31] The same terminology reviewed by Warner *et al.*[23] has been here adopted to address the various LSC figures of merit and their related quantities (Table S6;† for labelling of LSC slabs and relative devices see Table S4†). To derive the recommended LSC-PV reporting parameters from experimental data, we developed a Matlab Live Script that can be freely downloaded (see Data availability section).

The current density–voltage (*J–V*) characteristics of the LSC-PVs were investigated by illuminating the LSC active area and optically coupling one of its edges to two monocrystalline, single module Si cells with an active area of 2.2 × 0.7 cm^2 each. An apposite cell holder was designed to lodge the 0.27 cm thick LSC edge for the coupling, while covering the PV cell excess area to avoid any direct illumination from the light source. The uncoupled edges were masked with black tape and a matte black background was used.

The *J–V* curves are shown in Fig. 6a, while the short-circuit current density (J_{SC}), the open-circuit voltage (V_{OC}), the fill factor (FF), the maximum power (P_{MAX}) and the Power Conversion Efficiency (PCE, eqn (4)) are listed in Table 2.

$$\mathrm{PCE} = \frac{P_{out}}{P_{in}} = \frac{J_{SC} \times V_{OC} \times \mathrm{FF}}{P_0} \quad (4)$$

where P_{out} is the LSC-PV generated electrical power (W), P_{in} is the incident optical power (W), and P_0 indicates the incident power density ($P_{in} \times A_{in}$, see eqn (1) for A_{in} definition) expressed in mW cm^{-2}. Power–voltage (*P–V*) plots can be found in Fig. S5 of the ESI.†

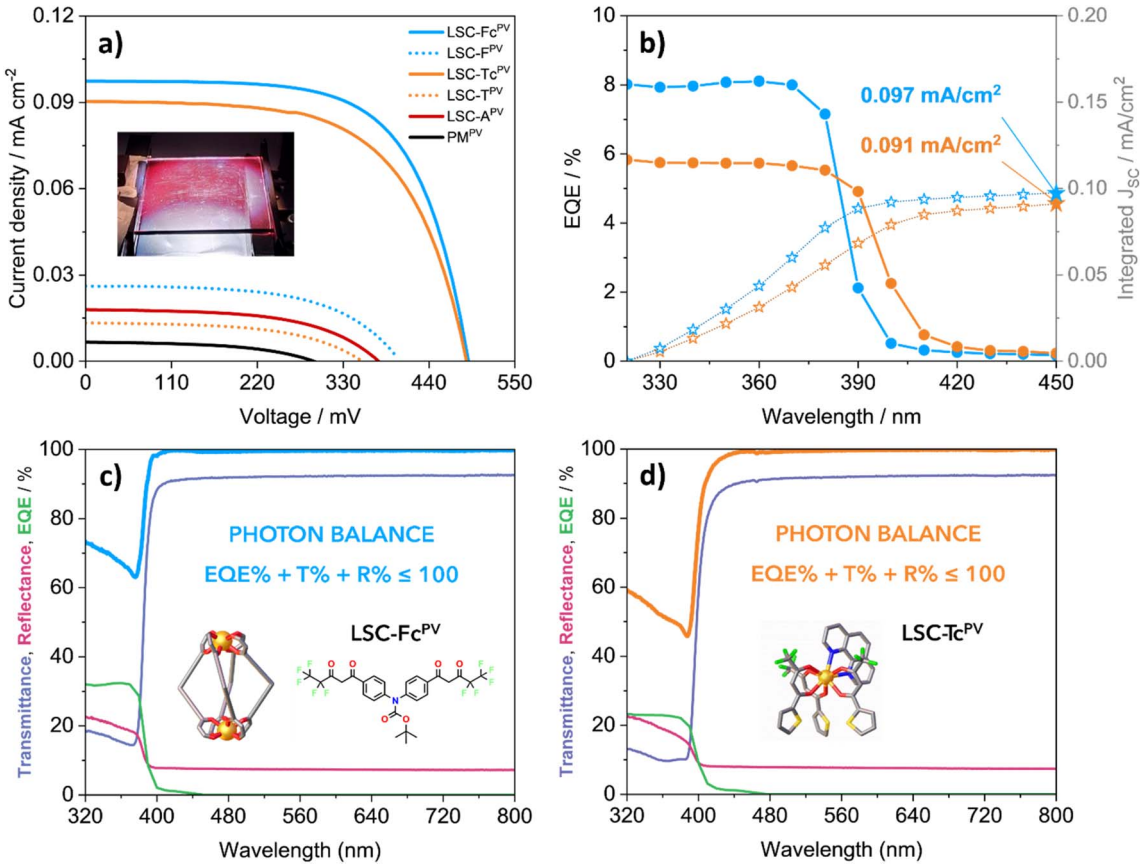

Fig. 6 (a) *J–V* curves recorded for the selected LSC-PVs with one PV coupled edge (inset: LSC-Fc under simulated AM1.5G irradiation). LSC-PV data of the undoped PMMA sample are reported for reference. (b) Experimental EQE spectra collected from one-edge measurements on **LSC-Fc^{PV}** and **LSC-Tc^{PV}** (solid lines) and corresponding integrated J_{SC} (dotted lines). (c and d) Consistency checks on the photon balance for **LSC-Fc^{PV}** and **LSC-Tc^{PV}** (insets: photon balance equation of the device and molecular structure of the embedded luminophore). Displayed EQE spectra (green lines) have been derived by applying a multiplicative correction factor of 4 to one-edge measurements.

Table 2 Short-circuit current density (J_{SC}), open-circuit voltage (V_{OC}), fill factor (FF), maximum power (P_{MAX}) and power conversion efficiency (PCE) values of tested LSC-PVs at higher luminophore loadings.

	J_{SC}/mA cm^{-2}						
	Experimental	Calculated from EQE[a]	V_{OC}/mV	FF	P_{MAX}/mW	PCE/% 1 edge (4 edges)[b]	η_{int}[c]/%
LSC-Fc^{PV}	0.097	0.097	490	0.65	0.780	0.031 (0.124)	55
LSC-Tc^{PV}	0.090	0.091	488	0.62	0.680	0.027 (0.108)	39
PM^{PV}	0.007	—	292	0.50	0.024	0.001 (0.004)	—

[a] Eqn (6). [b] Calculated by multiplying PCE by 4. [c] Defined in eqn (7) and (8).

The highest J_{SC}, V_{OC} and P_{max} values were observed for **LSC-Fc^{PV}** and **LSC-Tc^{PV}** indicating that higher luminophore loadings positively affect the electrical outputs. In particular, for **LSC-Fc^{PV}** we observed a maximum output power of 0.780 mW. PCE values for **LSC-Fc^{PV}** and **LSC-Tc^{PV}** stand one order of magnitude higher than those of **LSC-A^{PV}**, **LSC-F^{PV}** and **LSC-T^{PV}**.

We focus the following discussion on **LSC-Fc^{PV}** and **LSC-Tc^{PV}**, *i.e.*, on the best performing devices among the series. The data relative to the devices based on lower concentrated LSC tiles can be found in Table S7.†

The two doped samples produce comparable electrical outputs, with slightly better performance exhibited by **LSC-Fc^{PV}**. About 4% of the calculated PCEs arises from simple waveguiding of the incident white light by the PMMA matrix, as deduced from the study of the undoped LSC. Since *J*–*V* measurements were performed following the suggested guidelines, only one LSC edge has been coupled with solar cells. A multiplicative correction factor of 4 can be applied to estimate the energy that would be collected if all four edges were PV-coupled.[21] The recalculated PCE values would then equal to 0.124% and 0.108% for **LSC-Fc^{PV}** and **LSC-Tc^{PV}**, respectively. It is noteworthy that the former produces higher electrical outputs, even if by a small margin, than the latter although containing one fifth of its wt% concentration of luminophores.

Position dependent External Quantum Efficiency (EQE) spectra (Fig. 6b) have also been collected within the luminophores absorption range by means of a custom-built measurement station. The EQE of a photovoltaic device (eqn (5)) evaluates its capability to convert incident photons into charge carriers, and is proportional to the ratio between the produced electrical current ($I(\lambda)$) and the incident electrical power ($P(\lambda)$) at each given wavelength, also known as the spectral response (SR(λ)).

$$\mathrm{EQE}(\lambda)(\%) = 100 \times \frac{1240}{\lambda} \times \frac{I(\lambda)}{P(\lambda)} = 100 \times \frac{1240}{\lambda} \times \mathrm{SR}(\lambda) \quad (5)$$

By integration of the EQE over the AM1.5G spectrum, it is possible to estimate the short-circuit current density of the device under those illumination conditions (eqn (6)).

$$J_{SC} = e \times \int_s \mathrm{EQE}(\lambda) \times \Phi_{ph}^{AM1.5G}(\lambda)\mathrm{d}\lambda \quad (6)$$

When both EQE and *J*–*V* curves are available, a consistency check for LSC-PV devices can be performed by comparing the experimental J_{SC} value with that calculated from the EQE spectrum by means of eqn (6). This comparison is important because it reduces the possibility of photocurrent overestimation due, for example, to a non-perfect masking of the PV cell from direct illumination. Since such artifacts may be difficult to detect, this consistency check should be used to validate the measured data. Integrated J_{SC} values for **LSC-Fc^{PV}** and **LSC-Tc^{PV}** are reported in Fig. 6b and in Table 2. We found a very good agreement between experimental and integrated J_{SC} values, thus validating the experimental data and consequently the whole measurement setup. Furthermore, the good agreement between the measured and calculated J_{SC} values confirms the absence of scattering centres or particulates inside the waveguides, already assessed qualitatively by the naked eye and quantitatively through AVT determination.

The EQE spectra present similar shapes to the absorptance spectra and have the same absorption onsets (Fig. S6†). Any examined LSC-PV device should satisfy the photon balance $A(\lambda) + T(\lambda) + R(\lambda) = 1$ at all wavelengths, with $A(\lambda)$, $T(\lambda)$ and $R(\lambda)$ being the absorptance, transmittance and reflectance spectrum, respectively. Since the EQE(λ) quantifies how many of the incident photons on the LSC-PV generate a charge carrier pair, its value can at best match that of $A(\lambda)$, at each wavelength. Given the relation EQE(λ) $\leq A(\lambda)$, independent measurements of EQE, transmittance and reflectance should always satisfy the condition EQE(λ) + $T(\lambda)$ + $R(\lambda)$ $\leq$ 1.[21,32] This provides a useful consistency check for the photon balance of the device, which is fulfilled for both **LSC-Fc^{PV}** and **LSC-Tc^{PV}** (Fig. 6c and d).

After correction for the four sides, maximum EQE values become ≈32% at 360 nm and ≈23% at 320 nm for **LSC-Fc^{PV}** and **LSC-Tc^{PV}**, respectively. **LSC-Fc^{PV}** displays higher EQE than **LSC-Tc^{PV}**, which yields the larger integrated J_{SC} between the two LSC-PVs, and consequently the higher electrical output (Fig. 6a). Conversely, the latter has a lower EQE but a wider absorption range which allows it to capture an additional portion of the AM1.5G spectrum, wherein the photon population rapidly increases. This produces a *J*–*V* curve and a PCE value close to those of **LSC-Fc^{PV}**, despite the considerable gap between EQEs. Widening of absorption bands due to increased luminophore loadings is then a favourable factor for extracting more electrical power, provided that the LSC aesthetic quality is preserved. Further functionalization of $[Eu_2L_4]^{2-}$ cages oriented towards increased solubility in MMA could facilitate full utilization of the UV region by the proposed LSC-PVs.

Internal photon efficiency (η_{int}), defined in eqn (7) where n_{out} is the number of photons emitted at the edges and n_{abs} is the

number of photons absorbed from the active area, was derived from collected electrical parameters according to a verified method (eqn (8)).[23,33]

$$\eta_{int} = \frac{n_{out}}{n_{abs}} \quad (7)$$

$$\eta_{int} = \frac{I_{LSC\text{-}PV}}{I_{PV} \times G \times \eta_{s,abs}} \times \frac{\langle Q_s \rangle}{\langle Q_{PL} \rangle} \quad (8)$$

where $I_{LSC\text{-}PV}$, and I_{PV} are the short-circuit currents of the LSC-PV device and of the bare PV cell. Q_s and Q_{PL} are obtained by averaging the EQE of the PV cell over the AM1.5G or the luminophore emission spectrum.

Calculated internal photon efficiencies are 55% and 39% for **LSC-Fc^{PV}** and **LSC-Tc^{PV}**, respectively. Since η_{int} accounts for the optical losses of the sole LSC (*i.e.*, excluding the coupling to the photovoltaic component), scattering, PLQY and re-absorption are the three main factors contributing to this efficiency. Scattering and re-absorption losses have been found to be absent from our LSC-PVs, so the better η_{int} of **LSC-Fc^{PV}** is ascribed to the higher PLQY of $[Eu_2L^F_4]^{2-}$ with respect to Eu(tta)$_3$phen.

Furthermore, we performed some preliminary outdoor stability tests on **LSC-Fc** and **LSC-Tc** by exposing them, south-facing, to atmospheric ageing in Padova (Italy) from September to November 2023. During this period, the average temperature during the day went from 20–25 °C (Sep, Oct) to 15 °C (Nov). The average (2006–2022) Global Horizontal Irradiation (GHI) in Padova for September, October and November are 4.343, 2.737, and 1.542 kW h m^{-2}, respectively.[34] At sample retrieval, a drop in the measured I_{SC} of 20% and 30% was observed for **LSC-Fc** and **LSC-Tc**, respectively.

We finally compared the performance of our devices with that of other published Eu^{3+}-based concentrators (Table 3). Being recommended as the primary parameter to describe a LSC-PV, we chose the PCE as a metric for comparison.[23] To include precedent studies to the publication of the reporting guidelines,[21,23,31] where absent, PCE values have been calculated by us using experimental data provided in the cited references. To accurately compare PCE data, the device structure needs careful consideration: (i) the number of PV-coupled edges should be clearly specified, (ii) an efficient shielding from direct illumination on the edge-coupled photovoltaic cells and a matte black backdrop are required, and (iii) for measurements relative to one edge, the other three should be blackened. This configuration minimizes the contribution of stray light (light not generated by the LSC luminescence) to the photocurrent measurement.

Concerning the literature examples reported in Table 3, all the data are relative to one edge measurements, but device structures are quite different. While **Dev-A** has blackened edges and the backdrop is not specified, in **Dev-B** both edges and background are reflective. The edges of **Dev-C** are not taped and a white paper foil is used as reflective backdrop, allowing a 92% enhancement of the output power, as declared by the authors of the study.[36] To date, finding literature data on devices having analogous structures is quite demanding. The comparison between the results of our study and the literature shows that **LSC-Fc^{PV}** and **LSC-Tc^{PV}** produce electrical outputs of the same order of magnitude of most published Eu^{3+}-based LSC-PVs. This is a significant result, considering that the europium weight content of our devices (0.01 wt% for **LSC-Fc^{PV}** and 0.08 wt% for **LSC-Tc^{PV}**) is inferior to that found in the explored literature down to a one hundred factor.

The presented literature survey compares our LSC-PVs to other analogous Eu^{3+}-based systems with aesthetic properties (high transparency and lack of colour) comparable to ours. Interestingly, Jin *et al.*[37] recently reported LSCs with very similar aesthetic quality, based on a different type of emitter such as Ag,Mn:ZnInS$_2$/ZnS quantum dots (QDs). Moreover, this study followed the suggested reporting guidelines as well, allowing for a direct comparison of device metrics. The QD-based LSCs possess an AVT of 90% and CRI of 95.8, and has a PCE (4 edges) of 0.09%. Such values closely resemble our results, indicating that the devices herein developed rank competitively among the best UV-selective LSC technologies. Owing to the significantly higher intensity of solar radiation in the visible region compared to the ultraviolet region, LSCs based on UV absorbers inherently exhibit lower power conversion efficiencies than LSCs prepared employing visible absorbing luminophores.[6,23,38–42] However, this gain in PCE inevitably

Table 3 Survey of literature regarding Eu^{3+}-based LSCs, including for each publication the luminophore molecular structure, the employed matrix, the geometric gain (*G*), the device structure, the power conversion efficiency (PCE), and the weight concentration of europium with respect to the matrix.

	Luminophore	Matrix	*G*	Device structure	PCE/%	Eu^{3+}/wt%
This work	$[Eu_2L^F_4](NEt_4)_2$	PMMA	4.63	5.0 × 5.0 × 0.27 cm^3 bulk tile	0.031	0.01
This work	Eu(tta)$_3$phen	PMMA	4.63	5.0 × 5.0 × 0.27 cm^3 bulk tile	0.027	0.08
Dev-A (ref. 17)	Eu(tta)$_3$phen Eu(tta)$_3$Dpbt	Poly vinylbutyral (PVB)	6.50	Film (thickness not specified) deposited onto 7.8 × 7.8 × 0.3 cm^3 glass	0.044 0.050	0.24 0.20
Dev-B (ref. 19)	[B(TMSP)Im][Eu(tta)$_4$]	PMMA	7.85	5.1 μm thick film deposited onto 7.5 × 2.0 × 0.1 cm^3 glass	0.002	2.28
Dev-C (ref. 35)	Eu(2mCND)$_3$	Siloxane-polyether (di-ureasil)	2.89	320 μm thick film deposited onto 5.0 × 5.0 × 0.4 cm^3 acrylic	0.138[a]	1.05

[a] Value not reported in the publication, calculated based on provided experimental data.

comes at the expense of a decreased AVT and CRI, and therefore their applicability is strongly dependent on the context of use.

Conclusions

In conclusion, a series of highly transparent LSCs has been developed by incorporating a family of binuclear Eu^{3+} quadruple-stranded cages with bis-β-diketonate ligands, as well as a reference mononuclear Eu^{3+} β-diketonate, into PMMA. All the examined complexes retain their structural and photophysical characteristics throughout the study. However, it was possible to obtain viable LSCs only using $Eu(tta)_3phen$ and the $[Eu_2L_4]^{2-}$ cages bearing the L^A ligand and its functionalized version L^F. A minimal functionalization of the ligand determined a twenty-fold increase in the cage's solubility, which was a key factor in reaching higher luminophore loadings and consequently better light harvesting properties of the LSC.

The obtained LSCs appear highly transparent and colourless, with excellent visible transmission and colour rendering properties, comparable to those of widely industrialized glazing products. The increased $[Eu_2L^F{}_4]^{2-}$ loading makes **LSC-Fc^{PV}** the best performing sample in terms of PCE and EQE, with the latter exceeding 30% in the UV region. The increase in concentration does not affect transparency or colour neutrality of the material. The proposed materials are therefore promising for a seamless integration into buildings as photovoltaic windows, blocking UV light and producing energy while preserving functionality and aesthetics. Finally, the PCEs displayed by **LSC-Fc^{PV}** and **LSC-Tc^{PV}** are in line with those found in the literature regarding Eu^{3+}-based concentrators, but in our case the same performances are obtained with the use of a sensibly lower quantity of the lanthanide ion, down to two orders of magnitude less in terms of Eu^{3+} weight concentration. Particularly for **LSC-Fc^{PV}**, these results open the way for deployment of LSCs based on europium as highly transparent BIPVs while minimizing its usage.

Data availability

The Matlab Live Script for the calculation of recommended LSC-PV reporting parameters and a sample dataset to test the functionality of the script can be downloaded from the following link: **https://it.mathworks.com/matlabcentral/fileexchange/166426-luminescent-solar-concentrators-pv-characterization**.

Author contributions

Irene Motta; investigation, formal analysis, writing – original draft, writing – review & editing, software. Gregorio Bottaro; conceptualization, investigation, formal analysis, writing – original draft, writing – review & editing, software. Maria Rando; investigation, formal analysis, writing – review & editing. Marzio Rancan; conceptualization, investigation, formal analysis, writing – review & editing. Roberta Seraglia; investigation, formal analysis, writing – review & editing. Lidia Armelao; conceptualization, funding acquisition, supervision, writing – review & editing.

Conflicts of interest

The authors declare no conflict of interest.

Acknowledgements

This study is a result of the research project nuovi Concetti, mAteriali e tecnologie per l'iNtegrazione del fotoVoltAico negli edifici in uno scenario di generazione diffuSa' [CANVAS], funded by the Italian Ministry of the Environment and the Energy Security, through the Research Fund for the Italian Electrical System (type-A call, published on G. U. R. I. no. 192 on 18-08-2022). G. B. and M. R. thank the National Research Council PROGETTI@CNR P@CNR_01_TerMoSmart, FOE2020 'Capitale naturale e risorse per il futuro dell'Italia', FOE2022 FuturRaw. L. A. thanks the University of Padova P-DiSC#01-BIRD2021 for financial support. Dr Tobias Stürzer, Bruker AXS (Karlsruhe, Germany), is acknowledged for $\{[Eu_2L^F{}_4](NEt_4)_2\}$ single crystal X-ray data collection.

References

1 EC REPRESENTATIONS - European Green Deal: Commission proposes to boost renovation and decarbonisation of buildings, **https://ec.europa.eu/newsroom/representations/items/730847/default**, accessed December 30, 2023.
2 European Parliament, Council of the European Union, Directorate-General for Energy: Directive 2010/31/EU of the European Parliament and of the Council of 19 May 2010 on the Energy Performance of Buildings, *Off. J. Eur.Union*, 2010, **http://data.europa.eu/eli/dir/2010/31/oj**, accessed June 7, 2024.
3 C. J. Traverse, R. Pandey, M. C. Barr and R. R. Lunt, *Nat. Energy*, 2017, **2**, 849–860.
4 M. G. Debije and P. P. C. Verbunt, *Adv. Energy Mater.*, 2012, **2**, 12–35.
5 F. Meinardi, F. Bruni and S. Brovelli, *Nat. Rev. Mater.*, 2017, **2**, 17072.
6 B. S. Richards and I. A. Howard, *Energy Environ. Sci.*, 2023, **16**, 3214–3239.
7 R. A. S. Ferreira, S. F. H. Correia, A. Monguzzi, X. Liu and F. Meinardi, *Mater. Today*, 2020, **33**, 105–121.
8 J. Roncali, *Adv. Energy Mater.*, 2020, **10**, 2001907.
9 F. Meinardi, S. Ehrenberg, L. Dhamo, F. Carulli, M. Mauri, F. Bruni, R. Simonutti, U. Kortshagen and S. Brovelli, *Nat. Photonics*, 2017, **11**, 177–185.
10 C. Yang, M. C. Barr and R. R. Lunt, *Phys. Rev. Appl.*, 2022, **17**, 034054.
11 V. Fiorini, N. Monti, G. Vigarani, G. Santi, F. Fasulo, M. Massi, L. Giorgini, A. B. Muñoz-García, M. Pavone, A. Pucci and S. Stagni, *Dyes Pigm.*, 2021, **193**, 109532.
12 K. Lee, H.-D. Um, D. Choi, J. Park, N. Kim, H. Kim and K. Seo, *Cell Rep. Phys. Sci.*, 2020, **1**, 100143.

13 S. F. H. Correia, V. De Zea Bermudez, S. J. L. Ribeiro, P. S. André, R. A. S. Ferreira and L. D. Carlos, *J. Mater. Chem. A*, 2014, **2**, 5580–5596.
14 L. R. Wilson, B. C. Rowan, N. Robertson, O. Moudam, A. C. Jones and B. S. Richards, *Appl. Opt.*, 2010, **49**, 1651–1661.
15 K. Binnemans, in *Handbook on the Physics and Chemistry of Rare Earths*, Elsevier, 2005, vol. 35, pp. 107–272.
16 K. Wang, in *Rare Earth Coordination Chemistry*, John Wiley & Sons, Ltd, 2010, pp. 41–89.
17 X. Wang, T. Wang, X. Tian, L. Wang, W. Wu, Y. Luo and Q. Zhang, *Sol. Energy*, 2011, **85**, 2179–2184.
18 M. Tonezzer, G. Maggioni, A. Campagnaro, S. Carturan, A. Quaranta, M. della Pirriera and D. Gutierrez Tauste, *Prog. Photovoltaics*, 2015, **23**, 1037–1044.
19 A. R. Frias, M. A. Cardoso, A. R. N. Bastos, S. F. H. Correia, P. S. André, L. D. Carlos, V. de Zea Bermudez and R. A. S. Ferreira, *Energies*, 2019, **12**, 451.
20 L. Armelao, S. Quici, F. Barigelletti, G. Accorsi, G. Bottaro, M. Cavazzini and E. Tondello, *Coord. Chem. Rev.*, 2010, **254**, 487–505.
21 C. Yang, D. Liu and R. R. Lunt, *Joule*, 2019, **3**, 2871–2876.
22 C. Yang, H. A. Atwater, M. A. Baldo, D. Baran, C. J. Barile, M. C. Barr, M. Bates, M. G. Bawendi, M. R. Bergren, B. Borhan, C. J. Brabec, S. Brovelli, V. Bulović, P. Ceroni, M. G. Debije, J.-M. Delgado-Sanchez, W.-J. Dong, P. M. Duxbury, R. C. Evans, S. R. Forrest, D. R. Gamelin, N. C. Giebink, X. Gong, G. Griffini, F. Guo, C. K. Herrera, A. W. Y. Ho-Baillie, R. J. Holmes, S.-K. Hong, T. Kirchartz, B. G. Levine, H. Li, Y. Li, D. Liu, M. A. Loi, C. K. Luscombe, N. S. Makarov, F. Mateen, R. Mazzaro, H. McDaniel, M. D. McGehee, F. Meinardi, A. Menéndez-Velázquez, J. Min, D. B. Mitzi, M. Moemeni, J. H. Moon, A. Nattestad, M. K. Nazeeruddin, A. F. Nogueira, U. W. Paetzold, D. L. Patrick, A. Pucci, B. P. Rand, E. Reichmanis, B. S. Richards, J. Roncali, F. Rosei, T. W. Schmidt, F. So, C.-C. Tu, A. Vahdani, W. G. J. H. M. van Sark, R. Verduzco, A. Vomiero, W. W. H. Wong, K. Wu, H.-L. Yip, X. Zhang, H. Zhao and R. R. Lunt, *Joule*, 2022, **6**, 8–15.
23 T. Warner, K. P. Ghiggino and G. Rosengarten, *Sol. Energy*, 2022, **246**, 119–140.
24 M. Rancan, J. Tessarolo, A. Carlotto, S. Carlotto, M. Rando, L. Barchi, E. Bolognesi, R. Seraglia, G. Bottaro, M. Casarin, G. H. Clever and L. Armelao, *Cell Rep. Phys. Sci.*, 2022, **3**, 100692.
25 M. Rancan, M. Rando, L. Bosi, A. Carlotto, R. Seraglia, J. Tessarolo, S. Carlotto, G. H. Clever and L. Armelao, *Inorg. Chem. Front.*, 2022, **9**, 4495–4505.
26 S. Carlotto, L. Armelao and M. Rancan, *Int. J. Mol. Sci.*, 2022, **23**, 10619.
27 M. Pinsky and D. Avnir, *Inorg. Chem.*, 1998, **37**, 5575–5582.
28 K. Binnemans, *Coord. Chem. Rev.*, 2015, **295**, 1–45.
29 K.-L. Wong, J.-C. G. Bünzli and P. A. Tanner, *J. Lumin.*, 2020, **224**, 117256.
30 International Union of Pure and Applied Chemistry (IUPAC), **https://goldbook.iupac.org/terms/view/BT07338**, accessed June 7, 2024.
31 M. G. Debije, R. C. Evans and G. Griffini, *Energy Environ. Sci.*, 2021, **14**, 293–301.
32 C. Yang, D. Liu, M. Bates, M. C. Barr and R. R. Lunt, *Joule*, 2019, **3**, 1803–1809.
33 H. Li, K. Wu, J. Lim, H.-J. Song and V. I. Klimov, *Nat. Energy*, 2016, **1**, 16157.
34 Italian Solar Radiation Atlas, Italian National Agency for New Technologies, Energy and Sustainable Economic Development, ENEA, **https://www.solaritaly.enea.it/indexEn.php**, accessed May 23, 2024.
35 Y. Wang, Y. Liu, G. Xie, J. Chen, P. Li, Y. Zhang and H. Li, *ACS Appl. Mater. Interfaces*, 2022, **14**, 5951–5958.
36 Y. Liu, N. Li, R. Sun, W. Zheng, T. Liu, H. Li, Y. Chen, G. Liu, H. Zhao, H. Liu and Y. Zhang, *Nano Energy*, 2021, **85**, 105960.
37 L. Jin, E. Hamzehpoor, G. S. Selopal, J. Liu, P. Kumar, D. Benetti, X. Tong, D. F. Perepichka, Z. M. Wang and F. Rosei, *Small Methods*, 2024, 2301695.
38 M. Bartolini, C. Micheletti, A. Picchi, C. Coppola, A. Sinicropi, M. Di Donato, P. Foggi, A. Mordini, G. Reginato, A. Pucci, L. Zani and M. Calamante, *ACS Appl. Energy Mater.*, 2023, **6**, 4862–4880.
39 F. Meinardi, F. Bruni, C. Castellan, M. Meucci, A. M. Umair, M. La Rosa, J. Catani and S. Brovelli, *Adv. Energy Mater.*, 2024, **14**, 2304006.
40 J. Lin, L. Wang, Q. Jing and H. Zhao, *Chem. Eng. J.*, 2024, **481**, 148441.
41 X. Liu, D. Benetti, J. Liu, L. Jin and F. Rosei, *Nano Energy*, 2023, **111**, 108438.
42 C. Yang, M. C. Barr and R. R. Lunt, *Phys. Rev. Appl.*, 2022, **17**, 034054.